Hessam Babaee
e-mail: hbabae1@lsu.edu

Sumanta Acharya
Professor
e-mail: acharya@tigers.lsu.edu

Department of Mechanical Engineering,
Louisiana State University,
Baton Rouge, LA 70803

Xiaoliang Wan
Assistant Professor
Department of Mathematics,
Louisiana State University,
Baton Rouge, LA 70803
e-mail: xlwan@math.lsu.edu

Optimization of Forcing Parameters of Film Cooling Effectiveness

An optimization strategy is described that combines high-fidelity simulations with response surface construction, and is applied to pulsed film cooling for turbine blades. The response surface is constructed for the film cooling effectiveness as a function of duty cycle, in the range of DC between 0.05 and 1, and pulsation frequency St in the range of 0.2–2, using a pseudospectral projection method. The jet is fully modulated and the blowing ratio, when the jet is on, is 1.5 in all cases. Overall 73 direct numerical simulations (DNS) using spectral element method were performed to sample the film cooling effectiveness on a Clenshaw–Curtis grid in the design space. The geometry includes a 35-degree delivery tube and a plenum. It is observed that in the parameter space explored a global optimum exists, and in the present study, the best film cooling effectiveness is found at DC = 0.14 and St = 1.03. In the same range of DC and St, four other local optimums were found. The physical mechanisms leading to the forcing parameters of the global optimum are explored and ingestion of the crossflow into the delivery tube is observed to play an important role in this process. The gradient-based optimization algorithms are argued to be unsuitable for the current problem due to the nonconvexity of the objective function. [DOI: 10.1115/1.4025732]

1 Introduction

To enhance the thermal efficiency of a gas turbine, higher rotor inlet temperatures are desired requiring more effective cooling strategies of the components downstream. Film cooling of the high pressure turbine is commonly employed in modern turbine designs [1]. The coolant flow is extracted from the compressor and is bled through discrete film holes on the surface of the blade. The role of the coolant layer is to protect the components on the hot gas path and therefore increases the life of these components. The interaction between the coolant air and the mainstream causes aerodynamic losses in the turbine stage. In addition, coolant air represents a loss of the process air available for power or thrust. For these reasons one of the main objectives in cooling design is to use coolant as minimally as possible while ensuring a proper coverage of the coolant on the hot gas path components.

In order to improve cooling effectiveness, there have been a large number of studies that have explored hole shapes, blowing ratios (the ratio of the jet velocity to the crossflow velocity), coolant injection angles and other design parameters [1–3]. The majority of the studies that have explored parametric effects are either experimental or simulations that utilize the Reynolds-averaged Navier–Stokes (RANS) equations and a turbulence model. However, turbulence models in RANS have been shown to not capture the dynamics of the flow field accurately, and high-fidelity spatially and temporally resolved simulations that do not require models to capture the effects of the entire turbulent spectrum are needed [4]. Such techniques represented by direct numerical simulations (DNS), which resolves the entire spectrum, or large eddy simulations (LES), that captures the energetic parts of the spectrum, have indeed been recently employed in a number of film cooling studies [5–9]. Such high-fidelity simulations are used in the present work.

In recent years, pulsation of the coolant air has been suggested as one of the strategies that can possibly increase the film cooling effectiveness. Several researchers have studied the impact of pulsation on film cooling effectiveness, but the reported results have been mixed with no clear conclusive outcomes. Some key studies are reviewed below in order to motivate the present work.

Coulthard et al. [10] carried out an experimental study for an inclined jet with inclination angle of 35 deg. Their results show that the steady jet with BR of 0.5 resulted in the best film cooling effectiveness, and pulsations adversely impacted cooling effectiveness. Ekkad et al. [11] performed an experimental study in which they investigated the effect of pulsation on the film cooling effectiveness on a leading edge model for a variety of forcing parameters. At the lowest blowing ratio, BR = 0.75, the effect of pulsation was negligible. However, at higher blowing ratios pulsation had a positive effect on the film cooling effectiveness. They also observed that the pulsed jet outperformed the steady jet with the same time-averaged blowing ratio. El-Gabry and Rivir [12] studied the effect of pulsation on the leading edge film cooling on the same geometry [11], and observed that the film effectiveness of the pulsed cases were lower than that of steady jets with the same time-averaged blowing ratios.

Muldoon and Acharya [13] performed direct numerical simulations for St in the range of 0.004 to 0.32 and DC of 0.25 and 0.5. The baseline simulation was a steady jet at BR = 1.5. Pulsed cases at DC = 0.5 improved the film cooling effectiveness compared to the baseline case. The pulsed jet also showed improved film cooling effectiveness than a steady jet with the same effective mass flow rate, i.e., BR = 0.75.

Recently Bidan et al. [14] carried out an experimental/numerical study of a 35-deg jet in a crossflow. They observed that pulsation resulted in decrease of film cooling performance when compared against steady jets at the same mass flow rate. However, pulsated jets showed improvement of film cooling effectiveness when compared with steady cases with the same high blowing ratio.

It is clear from the studies above [10–14] that the reported results are not consistent with both positive and negative effects of coolant pulsations on film cooling. Further, in the experimental studies reported in the literature, there is a significant amount of deviation between the desired instantaneous blowing ratio and the actual delivered pulse form. This variability is usually more pronounced at higher frequencies. For instance, experimental

---

Contributed by the International Gas Turbine Institute (IGTI) of ASME for publication in the Journal of Turbomachinery. Manuscript received August 4, 2013; final manuscript received August 18, 2013; published online November 28, 2013. Editor: Ronald Bunker.

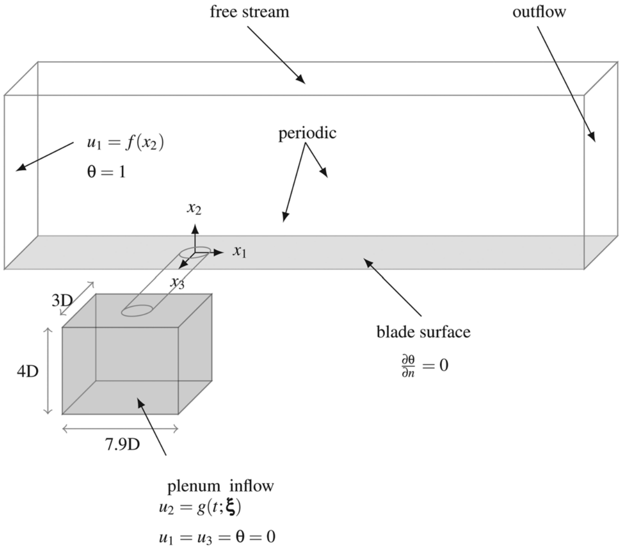

Fig. 1 Three-dimensional schematic of the jet in crossflow

measurements of Ref. [10] shows 100% deviation between the phased average blowing ratio at $\mathrm{St} = 0.19$ compared to the desired blowing ratio. In the experimental studies carried out by Refs. [12] and [14], significant amount of uncertainty, particularly at high St in Ref. [14], is reported. This variability in delivering the desired blowing ratio for the pulsed film cooling, however unavoidable, renders the task of comparing these studies cumbersome if not impossible, and this may, among other factors, explain the mixed results in the literature. Moreover, the majority of the studies to date have focused on preselecting the forcing frequency based on available hardware or on natural time scales in the flow. Thus, the parametric window exploring the role of pulsations have been limited, and it is possible that the optimal forcing frequency may be outside the preselected ranges considered.

Based on the results reported and the above arguments, it is clear that the role of pulsation on the cooling effectiveness needs to be better understood. In the current study, we perform controlled numerical experiments using high-fidelity direct numerical simulations for a wide range of pulsation frequencies ($\mathrm{St} \in [0.2, 2]$) and duty cycles ($\mathrm{DC} \in [0.05, 1]$). We extract the response surface of the system with respect to DC and St, and identify global and local optimums in the $\mathrm{DC} - \mathrm{St}$ space. In all of our simulations plenum and the delivery tube are included, since these are recognized to play an important role on the film cooling behavior [1–3]. To overcome the expensive computational cost of such a problem, we employ an efficient discretization strategy in the design space by using fast-converging spectral polynomials along with a high-order spectral/hp element method to carry out the direct numerical simulations. Within the range of parameters considered, a key goal of the paper is to find the optimal pulsation parameters, and to understand the mechanisms leading to the global optimal condition for film cooling effectiveness. A description of this optimization approach, and the corresponding results obtained for the film cooling cases are presented in this paper.

2 Methodology

We solve the incompressible Navier–Stokes equations without any use of a turbulence model by resolving all time and space scales. These equations in nondimensional form are

$$\frac{\partial \mathbf{u}}{\partial t} + (\mathbf{u} \cdot \nabla)\mathbf{u} = -\nabla p + \frac{1}{\mathrm{Re}}\nabla^2 \mathbf{u} \tag{1}$$

$$\nabla \cdot \mathbf{u} = 0 \tag{2}$$

where $\mathbf{u} = \mathbf{u}(\mathbf{x}, t; \boldsymbol{\xi})$ is the nondimensional velocity vector field and $p = p(\mathbf{x}, t; \boldsymbol{\xi})$ is the nondimensional pressure field in a space($\mathbf{x}$)-time (t) domain and $\boldsymbol{\xi} = (\xi_1, \xi_2)$ is a two-dimensional vector of *design* or *control parameters*. In the current study, design parameters are the duty cycle DC, and the nondimensional pulsation period $T_p = U_\infty / Df$, where U_∞ is the crossflow velocity, D is the jet diameter and f is the dimensional pulsation frequency. As it will be explained later in this section DC and T_p are related to ξ_1 and ξ_2 through a linear mapping. The Reynolds number is defined as $\mathrm{Re} = U_\infty D/\nu$, where ν is the kinematic viscosity. In order to calculate the heat transfer on the blade surface the energy equation for the incompressible flow is solved. This equation is given by

$$\frac{\partial \theta}{\partial t} + (\mathbf{u} \cdot \nabla)\theta = \frac{1}{\mathrm{RePr}}\nabla^2 \theta \tag{3}$$

where $\theta = \theta(\mathbf{x}, t; \boldsymbol{\xi})$ is the nondimensional temperature given by

$$\theta = \frac{T - T_c}{T_h - T_c} \tag{4}$$

Here T_c is the coolant temperature and T_h is the hot gas temperature.

Figure 1 shows the schematic of the problem. The velocity signal at the bottom of the plenum, $g(t; \boldsymbol{\xi})$, is fixed by specifying the design parameters (DC,T_p) and the maximum and minimum plenum-inflow velocity. In Fig. 2, the generic form of the signal $g(t; \boldsymbol{\xi})$ is shown. The amount of the time that the jet is on within each full period is denoted by Δt_{on} and therefore $\mathrm{DC} = \Delta t_{\mathrm{on}}/T_p$. We also introduce τ that shows the time percentage during a cycle. Therefore $\tau < \mathrm{DC}$ represents the period that the jet is on and $\tau > \mathrm{DC}$ when the jet is off. When the jet is on, the vertical velocity at the bottom of the plenum is equal to $\alpha\mathrm{BR}$. Here $\alpha = \pi D^2/4A_p$, with A_p being the area of the bottom of the plenum, accounts for the ratio of the area of the delivery tube to that of the plenum. When the jet is off, it is turned completely off and during this time the net mass flow rate through any x_2-section at the plenum or delivery tube is zero.

2.1 Optimization Problem.

Our objective is to maximize the film cooling effectiveness as a function of duty cycle and pulsation period. To measure the effectiveness of film cooling we first define the spanwise-averaged film cooling effectiveness which is given by

$$\eta(x_1; \boldsymbol{\xi}) = \frac{1}{w(t_f - t_i)} \int_{t_i}^{t_f} \int_{-w/2}^{w/2} (1 - \theta(\mathbf{x}, t; \boldsymbol{\xi}))|_{x_2=0} \mathrm{d}x_3 \mathrm{d}t \tag{5}$$

with w being the width of the cooled surface, t_i and t_f are the beginning and the end of the period over which the time-averaged quantities are calculated. In order to obtain an overall measure of the film cooling effectiveness, we further calculate the streamwise average of $\eta(x_1; \boldsymbol{\xi})$. This results

$$\tilde{\eta}(\boldsymbol{\xi}) = \frac{1}{x_{1_e} - x_{1_s}} \int_{x_{1_s}}^{x_{1_e}} \eta(x_1; \boldsymbol{\xi}) \mathrm{d}x_1 \tag{6}$$

where x_{1_s} and x_{1_e} are the two ends of the interval in the streamwise direction within which the average film cooling effectiveness is calculated. The overall film cooling effectiveness, $\tilde{\eta}(\boldsymbol{\xi})$, is a function of two independent variables DC and T_p, with BR and geometry fixed. The goal is to find the DC and T_p at which the average film cooling effectiveness, $\tilde{\eta}(\boldsymbol{\xi})$, is globally maximum, and to understand the reasons that lead to this condition.

2.2 Discretization in Space-Time.

We use spectral/hp element method implemented in $\mathbb{N}\varepsilon\kappa\mathbb{T}\alpha r$ by Warburton [15] to

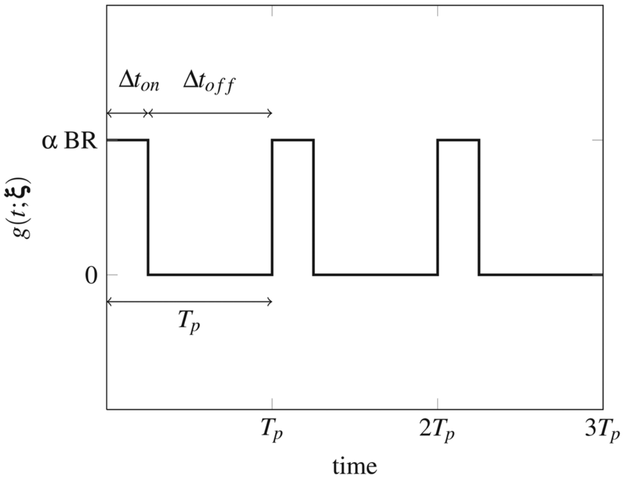

Fig. 2 Blowing ratio signal $g(t;\xi)$ specified as vertical velocity at the plenum inlet

perform direct numerical simulations of the incompressible Navier–Stokes equations along with the advection-diffusion equation for temperature given by Eqs. (1)–(3). For time advancement, the semi-implicit third-order fractional step method [16] is employed. In space unstructured hexahedral element with spectral order of three or four is used. More details of the spectral/hp element solver are given in Ref. [17].

2.3 Discretization in Design Parameter Space.

We intend to estimate the response surface for film cooling pulsation where the design parameters, DC and T_p, constitute a Cartesian two-dimensional space and the response surface is $f := f(\boldsymbol{x};\boldsymbol{\xi})$. Here, f is a generic time-averaged variable. In order to discretize the governing Eqs. (1)–(3) in the design space (ξ_1,ξ_2), we use pseudospectral method [18] to project $f(\boldsymbol{x};\boldsymbol{\xi})$ to a polynomial space. This follows

$$f(\boldsymbol{x};\boldsymbol{\xi}) = f_N(\boldsymbol{x};\boldsymbol{\xi}) + \varepsilon(\boldsymbol{x};\boldsymbol{\xi}) \tag{7}$$

with

$$f_N(\boldsymbol{x};\boldsymbol{\xi}) = \sum_{j=0}^{P_2}\sum_{i=0}^{P_1}\widehat{f_{ij}}(\boldsymbol{x})\phi_i(\xi_1)\phi_j(\xi_2) \tag{8}$$

where $\phi_i(\xi_1)$ and $\phi_j(\xi_2)$ are polynomials up to degree P_1 and P_2, respectively, and $\varepsilon(\boldsymbol{x};\boldsymbol{\xi})$ is the error of the expansion. For convenience we use a two-dimensional basis which is obtained by multiplying the univariate basis in each direction. This follows

$$\boldsymbol{\phi}_r(\boldsymbol{\xi}) = \phi_i(\xi_1)\phi_j(\xi_2), \quad 0 \le i \le P_1, \quad 0 \le j \le P_2 \tag{9}$$

where r is

$$r = i + j(P_1+1), \quad 0 \le i \le P_1, \quad 0 \le j \le P_2$$

Therefore $0 \le r \le N$ with $N = (P_1+1)(P_2+1) - 1$. Thus, Eq. (8) can be rewritten as

$$f_N(\boldsymbol{x};\boldsymbol{\xi}) = \sum_{i=0}^{N}\widehat{f_i}(\boldsymbol{x})\boldsymbol{\phi}_i(\boldsymbol{\xi}) \tag{10}$$

We use Legendre polynomials for their fast convergence for a smooth function f. We define an inner product and a norm given by

$$(f,g) := \int f(\boldsymbol{\xi})g(\boldsymbol{\xi})d\boldsymbol{\xi}, \quad \|f\| := (f,f)^{1/2} \tag{11}$$

Legendre polynomials form an orthogonal basis, and therefore

$$(\boldsymbol{\phi}_i,\boldsymbol{\phi}_j) = \delta_{ij}\gamma_j^2, \quad i,j = 0,1,2,\ldots,N \tag{12}$$

where $\gamma_j = \|\boldsymbol{\phi}_j\|$

The coefficients $\hat{f}_i(\boldsymbol{x})$ are obtained using Galerkin projection by taking the inner product of two sides of Eq. (10) with $\boldsymbol{\phi}_j$. Using the orthogonality relation of the Legendre polynomial given by Eq. (12), we have

$$\widehat{f_j}(\boldsymbol{x}) = \frac{\int f(\boldsymbol{x};\boldsymbol{\xi})\boldsymbol{\phi}_j(\boldsymbol{\xi})d\boldsymbol{\xi}}{\gamma_j^2}, \quad j = 0,1,2,\ldots,N \tag{13}$$

To calculate $\int f(\boldsymbol{x};\boldsymbol{\xi})d\boldsymbol{\xi}$, we use pseudospectral method [18] in which the integral is estimated using a quadrature rule. This follows

$$\int f(\boldsymbol{x};\boldsymbol{\xi})\boldsymbol{\phi}_j(\boldsymbol{\xi})d\boldsymbol{\xi} \simeq \sum_{i=1}^{Q}\mathbf{w}^{(i)}f(\boldsymbol{\xi}^{(i)})\phi_j(\boldsymbol{\xi}^{(i)}) \tag{14}$$

where $\boldsymbol{\xi}^{(i)}$ and $\mathbf{w}^{(i)}, i = 1,2,\ldots Q$ are quadrature points and weights in the two-dimensional space of design variables, respectively.

We use Clenshaw–Curtis nodes [19] which are the extrema of Chebychev polynomials and for a one-dimensional Chebyshev polynomial of order P are given by

$$\Theta^P = \left\{\cos\frac{2\pi i}{P}, i = 0,1\ldots,P\right\} \tag{15}$$

Using Clenshaw–Curtis nodes (Θ^P) results in accurate evaluation of expansion coefficients (Eq. (13)) and thus, leading to fast convergence of $f_N(\boldsymbol{x};\boldsymbol{\xi})$ to $f(\boldsymbol{x};\boldsymbol{\xi})$ for a smooth function f [20]. This fact is at the core of the efficiency of the method that we are using to discretize Eqs. (1)–(3) in the design space. Since evaluating at each sample point is in fact solving an expensive DNS simulation, our goal is to minimize the number of samples for a desirable accuracy.

Following the above notation, if the Clenshaw–Curtis nodes for a polynomial of order P in the ξ_i-direction are denoted by Θ_i^P, the Clenshaw–Curtis nodes in the two-dimensional design space are given by the full tensor product of the corresponding one-dimensional nodes in each direction. This follows

$$\Theta^{(P_1,P_2)} = \Theta_1^{P_1} \otimes \Theta_2^{P_2} \tag{16}$$

In this study we always use $P_1 = P_2 = P$, however, in general, they can be different. This results in $Q = (P+1)^2$ quadrature points in the design space. Note that

$$\xi_i \in [-1,1], \quad i = 1,2$$

A linear mapping is then used to transform ξ_i's to arbitrary intervals. This follows

$$\xi_i^* = \frac{1-\xi_i}{2}a_i + \frac{1+\xi_i}{2}b_i, \quad i = 1,2$$

where

$$\xi_i^* \in [a_i,b_i], \quad i = 1,2$$

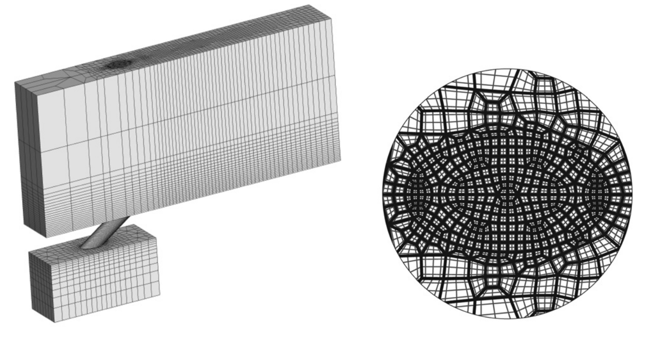
(a) (b)

Fig. 3 Unstructured hexahedral grid; (*a*) three-dimensional view; (*b*) $x_1 - x_3$ view of the grid in the vicinity of the jet exit with spectral order $m = 4$

In the current study ξ_1^* and ξ_2^* represent pulsation period (T_p) and duty cycle (DC) respectively. Now we can use a similar polynomial expansion as in the Eq. (10), to estimate the time-averaged quantities:

$$\bar{\mathbf{u}}_N(\mathbf{x};\boldsymbol{\xi}) = \sum_{k=0}^{N} \widehat{\bar{\mathbf{u}}}_k(\mathbf{x})\boldsymbol{\phi}_k(\boldsymbol{\xi}) \tag{17}$$

$$\bar{p}_N(\mathbf{x};\boldsymbol{\xi}) = \sum_{k=0}^{N} \widehat{\bar{p}}_k(\mathbf{x})\boldsymbol{\phi}_k(\boldsymbol{\xi}) \tag{18}$$

$$\bar{\theta}_N(\mathbf{x};\boldsymbol{\xi}) = \sum_{k=0}^{N} \widehat{\bar{\theta}}_k(\mathbf{x})\boldsymbol{\phi}_k(\boldsymbol{\xi}) \tag{19}$$

where the expansion coefficients are obtained from

$$\hat{\bar{\mathbf{u}}}_k(\boldsymbol{x}) = \sum_{i=1}^{Q} \mathbf{w}^{(i)}\mathbf{u}(\boldsymbol{x};\boldsymbol{\xi}^{(i)})\boldsymbol{\phi}_k(\boldsymbol{\xi}^{(i)})/\gamma_k^2, \quad 0 \le k \le N \tag{20}$$

$$\widehat{\bar{p}}_k(\boldsymbol{x}) = \sum_{i=1}^{Q} \mathbf{w}^{(i)}p(\boldsymbol{x};\boldsymbol{\xi}^{(i)})\boldsymbol{\phi}_k(\boldsymbol{\xi}^{(i)})/\gamma_k^2, \quad 0 \le k \le N \tag{21}$$

$$\widehat{\bar{\theta}}_k(\boldsymbol{x}) = \sum_{i=1}^{Q} \mathbf{w}^{(i)}\theta(\boldsymbol{x};\boldsymbol{\xi}^{(i)})\boldsymbol{\phi}_k(\boldsymbol{\xi}^{(i)})/\gamma_k^2, \quad 0 \le k \le N \tag{22}$$

Similarly, $\tilde{\eta}(\boldsymbol{\xi})$ is approximated using the polynomial expansion. This follows

$$\tilde{\eta}_N(\boldsymbol{\xi}) = \sum_{k=0}^{N} \widehat{\tilde{\eta}}_k\boldsymbol{\phi}_k(\boldsymbol{\xi}) \tag{23}$$

Using Eqs. (5), (6), and (23), it is easy to verify that

$$\hat{\tilde{\eta}}_k = 1 - \frac{1}{w(x_{1_e} - x_{1_s})}\int_{-w/2}^{w/2}\int_{x_{1_s}}^{x_{1_e}} \widehat{\bar{\theta}}_k(\mathbf{x})|_{x_2=0}\,dx_1 dx_3 \tag{24}$$

3 Simulation Details

In all the cases in this study we perform direct numerical simulation on the jet in crossflow with the schematic of the problem shown in Fig. 1. The origin of the coordinate system is at the center of the jet exit and x_1 is aligned with the streamwise direction, x_2 with the direction normal to the cooled surface and x_3 with the spanwise direction. The plenum has the length, height and width of 7.9D, 4D and 3D, respectively. The length of the delivery tube is 3.5D and the inclination angle is 35 deg. The mainstream domain, where the crossflow and the coolant interact, spans the volume with the size of 22D × 10D × 3D. The center of the jet exit is located 7D downstream from the crossflow inlet. The crossflow boundary condition is assumed to be a laminar boundary layer flow with boundary layer thickness of $\delta_{99\%}/\mathrm{D} = 0.5$, where $\delta_{99\%}$ is the thickness at which the streamwise velocity in the boundary layer reaches 99% of the free-stream velocity. On the top boundary plane, free-stream flow is assumed with $\mathbf{u}(x_1, 10, x_3) = (U_\infty, 0, 0)$ and $\theta(x_1, 10, x_3) = 1$, and on the spanwise direction periodic boundary condition is enforced. The periodic boundary condition mimics the situation where a row of holes are arranged in the spanwise direction. In the current case, the center-to-center distance between two consecutive holes is 3D. A zero normal derivative boundary condition is assumed at the outflow. The uniform boundary condition $g(t;\boldsymbol{\xi})$ (see Fig. 2) is used for the vertical velocity component u_2 at the bottom of the plenum with $u_1 = u_3 = 0$ and $\theta = 0$. The area scaling factor is $\alpha = 0.0331$. As noted earlier, each pair of the design variables (DC, T_p), and the peak blowing ratio (the blowing ratio when the jet is on and is set to 1.5) specifies the signal $g(t;\boldsymbol{\xi})$. The Reynolds number, $\mathrm{Re}_j = U_j D/\nu$, based on the jet space-averaged velocity (when the jet is on) is 1500 throughout and Prandtl number is $Pr = 1$. For all the wall boundaries, adiabatic condition is assumed for temperature. The computational time step was roughly 0.001. All simulations were advanced at least $40\mathrm{D}/U_\infty$ before the statistics are collected. The statistics are then collected for approximately another $40\mathrm{D}/U_\infty$. Care was taken to ensure that the calculation of the statistics starts at the beginning of a pulsation cycle and finishes at the end of another pulsation cycle. Additional sampling did not change the result.

3.1 Computational Mesh. We use hexahedral elements of spectral order of three and four in the current simulations. Figure 3 shows the three-dimensional view of the grid. To generate the grid, quadrilateral meshes were first generated in the $x_1 - x_3$ planes in the main-stream domain, the delivery tube and the plenum. The quadrilateral elements exactly match across the common faces in between the volume parts. The two-dimensional mesh was then swept along the x_2 direction in the mainstream domain and plenum and along the axis of the cylinder in the delivery tube. The height of the first element in the crossflow boundary layer is 0.06D. The height of the elements increases (with 16 elements) using hyperbolic distribution to 0.3D at $x_2 = 4$. Two elements were used from $x_2 = 4$ to the top boundary at $x_2 = 10$. Note that flow in this region remains steady with small gradients which justifies using large elements. Along the delivery tube, 16 elements with uniform distribution were used. The finest elements are found in the delivery tube, especially in the boundary layer region where flow is highly unsteady with steep gradients. A close $x_1 - x_3$ view of the mesh in the vicinity of the jet exit is shown in Fig. 3. In the plenum, 11 elements were used in the x_2 direction with $\Delta x_2 = 0.06\mathrm{D}$ for the topmost elements and $\Delta x_2 = 0.12\mathrm{D}$ for the first element in the bottom. The elements in between were distributed using hyperbolic distribution. In total, 48,162 hexahedral elements were created. In each element spectral polynomials with order three or four were used. This amounts to a total degree of freedom of 3.1×10^6s for spectral order three, and 6.0×10^6 for spectral order of four.

In the design space, we use polynomial order up to degree $P = 8$ for each design variable. This results in $(P+1)^2 = 81$ points in the design space. In total, 73 DNS runs were performed, each on 56 processors and for six days. For all of the simulations studied in this work, roughly 600,000 CPU hours were consumed.

3.2 Convergence in Space and Time. To study the dependence of the numerical solution to grid resolution, we considered four simulations whose specifications are shown in Table 1. As a refinement strategy, we increased the spectral order of the mesh from three to four. As explained in the previous section, the mesh with spectral order four has almost twice as many degrees of

Table 1 Specification of the number of elements and polynomial order for cases considered in the grid study

	Case I	Case II	Case III	Case IV
Element size	48162	48162	48162	48162
Spectral order	3	4	3	4
T_p	2.75	2.75	Steady	Steady
DC	0.52	0.52	1	1

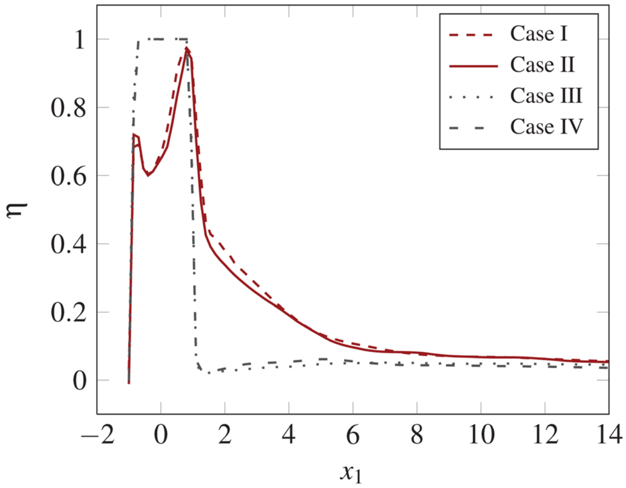

Fig. 4 Grid convergence study. The centerline film cooling effectiveness for cases shown in Table 1 are compared.

freedom as that of with the spectral order three. The centerline film cooling effectiveness for all four simulations are shown in Fig. 4. The comparisons are extended to also include the hole exit. The results show a consistent agreement in all cases considered. In the rest of this study, we use elements with spectral order three which provides proper resolution for the current problem.

3.3 Convergence in Design Space. To study the convergence of the polynomial expansion for film cooling effectiveness, we project $\tilde{\eta}(\xi)$ to the polynomial expansion given by Eq. (23) for increasing polynomial order, ranging from $P = 0$ to $P = 8$. Since we use equal polynomial order in ξ_1 and ξ_2 directions; therefore $N = (P+1)^2 - 1$ and by varying P, N changes accordingly. To measure the contribution by increasing polynomial order from $P-1$ to P, we calculate the modules $m(P)$ as in the following:

$$m(P) = \left(\sum_{k=0}^{(P+1)^2} \gamma_k^2 \widehat{\tilde{\eta}}_k^2 - \sum_{k=0}^{P^2} \gamma_k^2 \widehat{\tilde{\eta}}_k^2 \right)^{1/2} \qquad 1 \le P \le 8$$

$$m(P) = \gamma_0 |\widehat{\tilde{\eta}}_0| \qquad P = 0 \qquad (25)$$

Here the $\widehat{\tilde{\eta}}_k$'s are the expansion coefficients in overall cooling effectiveness given by Eq. (24), and γ_k's are used as a normalizing factor for the Legendre polynomials. The modules $m(P)$ versus P is shown in Fig. 5. The most significant contributions to the response surface are gained from polynomials in the range of $P = 0$ to $P = 3$. Larger polynomial contributions have modules of the same order, but almost one order smaller than those of lower polynomial orders. The main reason that the modules for the higher-order polynomials do not decay as fast as those of lower-order is the nonmonotonic behavior of the average film cooling effectiveness versus DC and T_p. However the improvement of the response surface by increasing the polynomial order is marginal ($O(10^{-3})$) and the behavior of the surface is essentially the same. Note that further increase in polynomial order requires prohibitively expensive DNS computations, while marginally modifying the response surface. In the rest of this study, we consider the response surface with polynomial order $P = 8$.

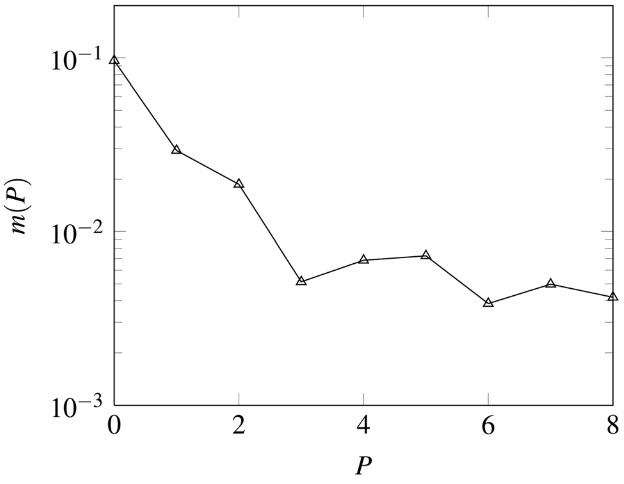

Fig. 5 Error convergence for $\tilde{\eta}_N(\xi)$ with increasing polynomial order

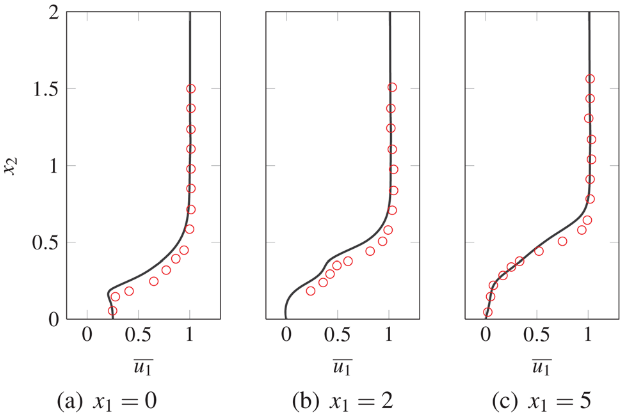

(a) $x_1 = 0$ (b) $x_1 = 2$ (c) $x_1 = 5$

Fig. 6 Comparison of time-averaged u_1 velocity in the midplane with experimental data [21] at BR = 0.15

4 Results and Discussions

As validation, we compare the results obtained from our direct numerical simulation with the experimental measurements carried out by Bidan et al. [21] for a 35-deg inclined jet in crossflow. The computational domain consists of a pipe with length of 7D with a 35-deg angle with the crossflow and a mainstream domain that expands the volume of 21D in the streamwise direction, 10D in the wall-normal direction and 6D in the spanwise direction. The Reynolds number based on the crossflow velocity and the boundary layer thickness is $\mathrm{Re}_\infty = U_\infty \delta / \nu = 1710$. The crossflow has a laminar boundary layer profile with a boundary layer thickness of 0.63D. At the pipe inlet uniform flow is superposed with 10% turbulence, generated by employing the spectral synthesizer method introduced in Ref. [22]. A hexahedral grid with 121,700 elements with a spectral polynomial degree of 4 is used. The comparisons are made for a continuous case with BR = 0.15. In Fig. 6, time-averaged streamwise velocity profiles are compared with those of experimental measurements in Ref. [21] at three different streamwise sections on the centerline plane. Overall good agreement is obtained. This along with the result of the convergence studies that was presented in the previous section give us confidence in carrying out the computations with the current approach.

4.1 Effect of Pulsation on Film Cooling Performance.

In examining these results, it is important to remember that the blowing ratio fluctuates between 1.5, when the valve is open, and 0, when the valve is closed, and any comparisons with the steady $\mathrm{BR} = 1.5$ case is, therefore, not at a constant coolant mass injection rate when integrated over a time duration. For the pulsed cases, the integrated coolant injection rates are lower, and an equal or greater cooling effectiveness than the baseline steady jet of $\mathrm{BR} = 1.5$ represents an improvement in the cooling strategy. We choose the pulsation period to be in the range of $T_p \in [0.5, 5]$, which corresponds to Strouhal number in the range of $\mathrm{St} \in [0.2, 2]$, and duty cycle in the range of $\mathrm{DC} \in [0.05, 1]$. All the sampling points with $\mathrm{DC} = 1$ correspond to a steady jet and, therefore, only one simulation was performed for these points.

Figure 7 shows the nondimensional temperature at the x_2-plane which represents the cooling effectiveness on the surface and the flow temperature at the exit of the coolant hole. As noted earlier, the two control parameters being varied include the duty cycle (DC) and the time period of pulsation (T_p) which is inversely proportional to frequency or Strouhal number. The rightmost column represents the steady blowing condition at a BR of 1.5. The signature of the near-hole jet blow-off and the downstream spread of the coolant jet on the surface can be seen. Both duty cycle and time period have important and significant influence on the cooling effectiveness. In Fig. 7, it is observed that the cooling effectiveness generally improves at a lower duty cycle (which represents a lower amount of integrated coolant injection) and higher frequencies, and that optimal conditions exist with global maximum in the lower left quadrant of the $\mathrm{DC} - T_p$ design space within the range of design parameters considered. However, the integrated values of the cooling effectiveness do not show any distinct linear or monotonic behavior in the design space, and local maxima or peaks are obtained at other points as shown later in Fig. 14. More discussions on the mechanisms leading to the global maximum are discussed in the next section for the case with $\mathrm{DC} = 0.09$ and $T_p = 1.16$, which is a point close to the global-maximum condition. In Fig. 8 the temperature distributions at $T_p = 1.16$ for increasing DC from 0.09 to 1 (steady injection) are shown. One can see that in the baseline condition ($\mathrm{DC} = 1$), the coolant jet is characterized by unsteady vortical structures that entrain and mix out the crossflow. The crossflow penetration to the surface is clearly evident in the longitudinal structures at elevated temperatures near the surface. As DC is reduced from 1, the turbulent structures and the near-wall thermal field are clearly influenced, with the lower duty cycles showing better organized structures and lower temperatures (presence of more coolant) near the wall. For DC larger than 0.34, the jet lift-off is observed immediately after entering the main domain resulting in poor coverage of the surface; this can also be seen in Fig. 7 where both the lateral and streamwise coverage of the coolant is poor. As DC is further decreased the coolant remains close to the surface and the crossflow entrainment under the coolant jet and close to the surface is reduced, and therefore lower coolant temperatures near the surfaces are observed. Thus the film cooling provides an effective coverage. These observations translate to higher cooling effectiveness as it is also observed in Fig. 7. Further discussions on why the lower DC's (where the integrated coolant mass flow rate is lower) leads to improved cooling effectiveness is provided later, and is related to the interaction between the mainstream and the coolant flow leaving the delivery tube. Figure 9 shows the instantaneous temperature distribution in the vertical midplane ($x_3 = 0$) at $\mathrm{DC} = 0.52$ with increasing time periods from 0.67 to 5. At higher time periods of $T_p \geq 1.89$, the coolant jet exhibits discrete vortex rings that are formed during the on-portion of the pulsation cycle. The same vortex structures were also recognized by Sau and Mahesh [23] for a pulsed vertical jet. These vortex rings are responsible for carrying the coolant flow downstream of the jet hole. The distance between successive vortex rings increases as the pulsation frequency decreases or the time period increases. Note that the instantaneous blowing ratio during the on-portion of the cycle is $\mathrm{BR} = 1.5$ which roughly becomes the velocity at which the vortex rings are convected along the axis of the delivery tube (35 deg with x_1). As a result, in Fig. 9, a distance of $d = 1.5T_p$ can be observed between two successive vortex rings. Since BR and DC remain unchanged for all the cases shown in

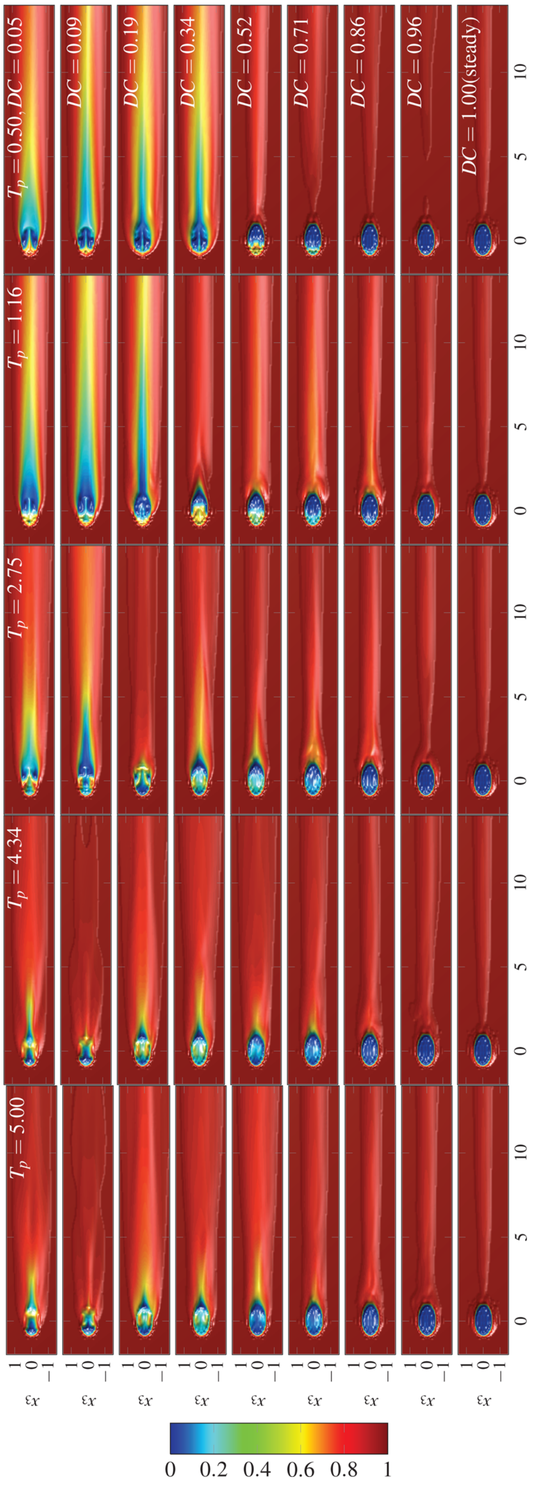

Fig. 7 Time-averaged temperature contours for quadrature points on cooled surface ($x_2 = 0$). Each row: constant T_p; each column: constant *DC*.

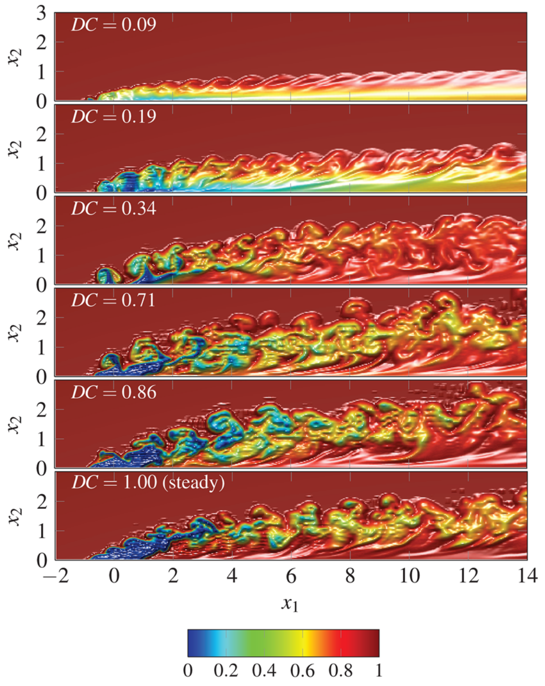

Fig. 8 Instantaneous temperature surface in the midplane ($x_3 = 0$) with constant pulsation period of $T_p = 1.16$. Plenum and delivery tube are not shown.

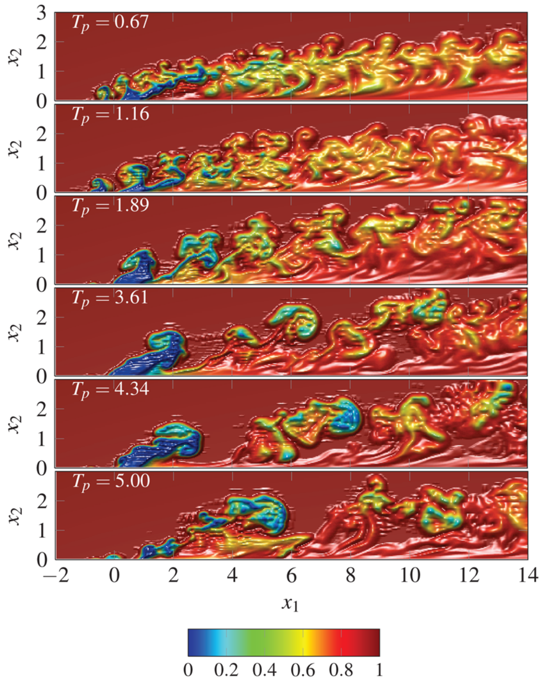

Fig. 9 Instantaneous temperature surface in the midplane ($x_3 = 0$) with constant duty cycle of DC = 0.52. Plenum and delivery tube are not shown.

Fig. 9, the higher pulsation period translates to more amount of the injected coolant, leading to the formation of larger and stronger vortex rings and greater instantaneous vertical-penetration. A visible trailing column can be seen for $T_p \geq 3.61$. For the case with $T_p = 4.34$ the upper shear layer shows strong oscillations, caused by the traveling vortices created when the flow leaves the plenum and enters the delivery tube and undergoes a sharp turn. As a result, an unsteady separation bubble forms in the upstream side of the tube, generating vortical structures that for a large enough pulsation period, such as $T_p = 4.34$, can travel the pipe length of 3.5D and affect the upper shear layer; a phenomenon that is absent in smaller pulsation periods.

4.2 Optimal and Suboptimal Behavior. In this section we investigate three cases in more details. In the previous section it was clear that lower duty cycle and high pulsation frequency (lower T_p) leads to higher film cooling effectiveness. The first case that we consider has DC = 0.09 and $T_p = 1.16$ which lies in the high film-cooling-effectiveness region in the design space and shows near-optimal film cooling performance (see Fig. 14). Temperature contours at four time instants of one pulsation cycle for this case are shown in Fig. 10. Note that τ represents the percentage of time during each cycle with $\tau = 0\%$ being the beginning and $\tau = 100\%$ the end of the cycle, and thus for $\tau < \mathrm{DC}$ the jet is on and for $\tau > DC$ the jet is completely off. At $\tau = 4\%$ the jet is on and the injected coolant initiates hairpin vortices (shown by arrows in Fig. 10) in the shear layer. The hairpin vortices are periodically generated and convected downstream. As the valve closes at $\tau = 9\%$, the crossflow enters the delivery tube from the leading edge of the hole, pushing the coolant in the delivery tube towards the downstream side of the hole and the coolant leaves the tube from the downstream edge of the hole (this adjustment in the exit flow is driven by mass conservation since the plenum-inflow was abruptly shut off). The ingestion of the crossflow into the delivery tube continues by forming a vortex ring that is clearly visible in the tube and near the exit at $\tau = 34\%$ and $\tau = 64\%$. The ingested gas reaches very close to the opposite wall of the delivery tube at $\tau = 94\%$. Note that the speed of the propagation of the vortex ring inside the delivery tube is slightly less than the nondimensional crossflow velocity of one (due to entrainment), and during the off-portion of the cycle with nondimensional $\Delta t_{\mathrm{off}} = 1.06$ (corresponding to DC of 0.09), the vortex ring has long enough time to travel one nondimensional unit of length (tube diameter) across the delivery tube and nearly reaches the opposite wall ($\tau = 94\%$). However, due to the short pulsation period, the plenum inflow is re-initiated before the ingested flow penetrates fully to the downstream-edge of the delivery tube, and before the ingested crossflow gas can cause a significant temperature rise in the interior wall of the delivery tube; this can be seen at the beginning of the new cycle at time $\tau = 4\%$ in Fig. 10. Other than the hairpin vortices, the steady presence of a counter rotating vortex pair (CRVP) is observed. Figure 11 shows the lateral-vertical velocity vectors at two streamwise sections. A double-deck vortex pair is observed with the lower deck showing the CRVP and the upper deck is resulted by crossing the hairpin vortex legs. The velocity field that is induced by each pair of these vortex structures tend to lift the jet off the surface (see for example Ref. [24]) and unfavorably affects the cooling performance. The amount of the induced vertical velocity, however, is directly proportional to the strength of the vortex pair which is supplied by the amount of the coolant injection. Due to both short duty cycle (DC = 0.09) and pulsation period ($T_p = 1.16$), the induced vertical velocity for this case is small (0.01 of the crossflow velocity) resulting in slow rise of the coolant from the surface (see the first image in Fig. 8) and thus providing an effective coverage of the surface.

The second case we discuss here is the pulsed film cooling with higher duty cycle of DC = 0.34 compared to the first case and with the same pulsation period of $T_p = 1.16$. Four snapshots during one pulsation period are shown in Fig. 12. The top images show the injection of the coolant into the crossflow. The coolant forms a vortex ring that gains more strength as time progresses during the on-portion of the cycle and the size of the vortex ring increases from $\tau = 10\%$ to $\tau = 27\%$. In this case larger duty cycle injects more coolant mass during the on-period and allows the complete formation of a vortex ring, an observation in contrast with the case at DC = 0.09 where the smaller duty cycle is not long enough to allow the formation of vortex rings during the

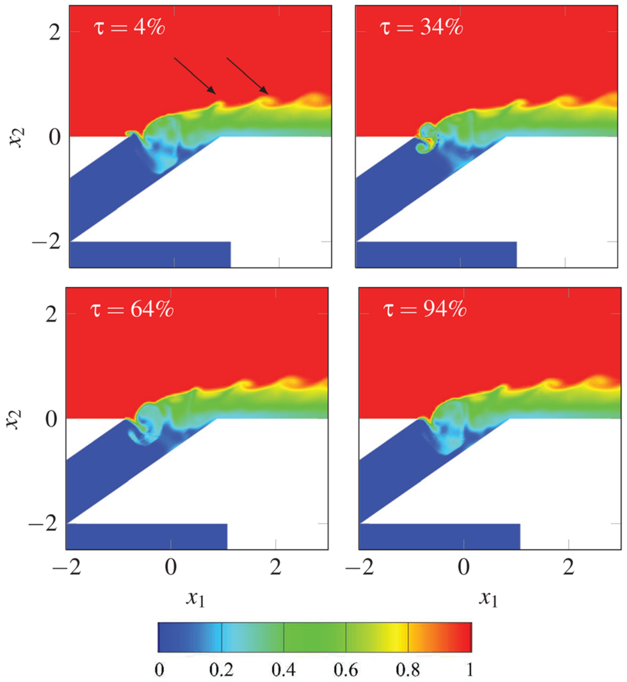

Fig. 10 Snapshots of instantaneous temperature at $x_3 = 0$ during one pulsation cycle with DC = 0.09, $T_p = 1.16$, $\Delta t_{\rm on} = 0.10$ and $\Delta t_{\rm off} = 1.06$

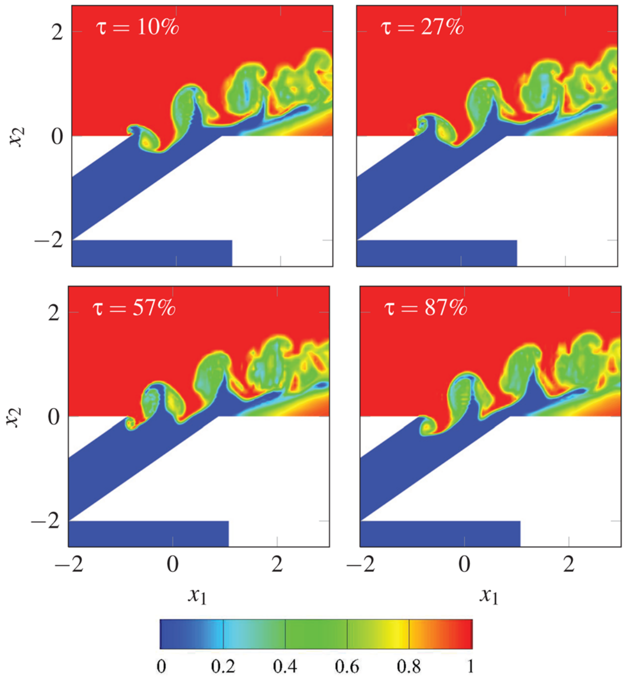

Fig. 12 Snapshots of instantaneous temperature at $x_3 = 0$ during one pulsation cycle with DC = 0.34, $T_p = 1.16$, $\Delta t_{\rm on} = 0.39$ and $\Delta t_{\rm off} = 0.77$

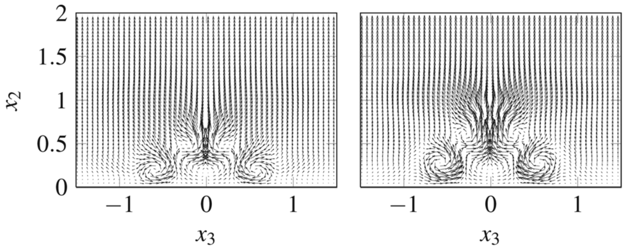

Fig. 11 Instantaneous $u_2 - u_3$ velocity vector field at: left $x_1 = 2$; right $x_1 = 4$, at DC=0.09 and $T_p = 1.16$

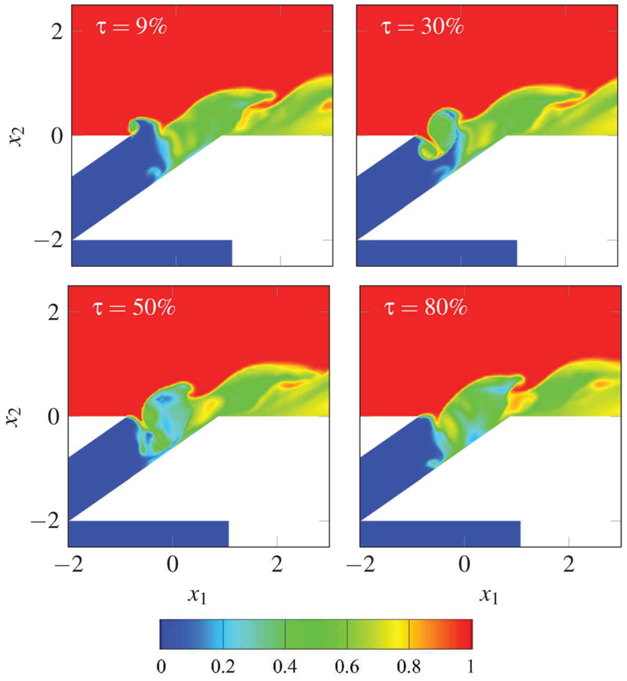

Fig. 13 Snapshots of instantaneous temperature at $x_3 = 0$ during one pulsation cycle with DC = 0.09, $T_p = 2.75$, $\Delta t_{\rm on} = 0.25$ and $\Delta t_{\rm off} = 2.5$

injection time. The vortex rings, which carry significant amount of the coolant, penetrate into the mainstream flow and are separated from the surface; thus allowing the entrainment of the crossflow to the surface below the jet. This leads to poor coverage of the surface as it can be seen in Fig. 7. During the off-portion of the cycle the initial stages of the crossflow ingestion into the delivery tube can be observed in Fig. 12 at $\tau = 57\%$ and $\tau = 87\%$ by the rolling up inside the hole. However, due to the low pulsation period ($T_p = 1.16$) and small nondimensional time length in the off-portion of the cycle ($\Delta t_{\rm off} = 0.77$), the hot gas cannot reach the tube walls before the next cycle begins. This shows that despite the ingestion of the hot gas into delivery tube, the wall temperature does not increase.

The third case investigated in this work is at DC $= 0.09$ and $T_p = 2.75$, which has the same duty cycle as that of the first case but higher pulsation time period. Four instants of temperature contours during one cycle are shown in Fig. 13. During the on-portion of the cycle ($\tau = 9\%$), a starting vortex forms which gains more strength compared to that of the first case (due to the longer $\Delta t_{\rm on}$ for this case) and grows larger in size, entraining more amount the hot mainstream flow, leading to increased mixing. During the off-portion of the cycle, a vortex ring similar to the first case forms, causing the ingestion of the crossflow into the delivery tube. The longer amount of the pulsation period ($\Delta t_{\rm off} = 2.50$) compared to the first case ($\Delta t_{\rm off} = 1.06$) gives the ingested gas enough time to impinge to the tube wall, causing significant increase in the wall temperature. Between two successive pulses, the crossflow penetrates to the delivery tube surface due to larger lapses between the coolant pulses and thus adversely affecting the cooling coverage.

The last two cases demonstrate the mechanisms that are responsible for the deterioration of the film cooling effectiveness when either duty cycle or pulsation period increases with respect to the

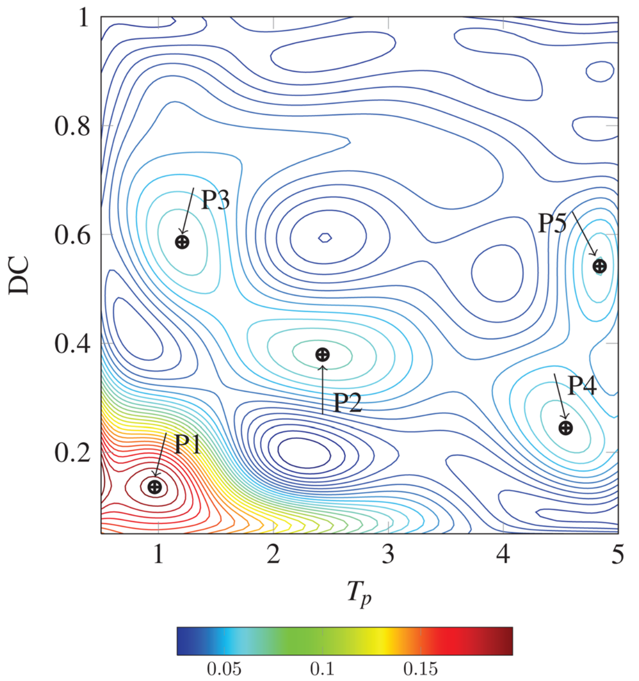

Fig. 14 Contours of averaged film cooling effectiveness ($\tilde{\eta}_N(\xi)$). Local and global maxima are shown, with P_1 being the global maximum and P_2 to P_5 are local maxima ordered with decreasing values.

Table 2 Local and global optimal design points

Point	DC	T_p	St	$\tilde{\eta}_N(\xi)$
P1	0.14	0.97	1.03	0.18
P2	0.38	2.43	0.41	0.08
P3	0.56	1.21	0.83	0.076
P4	0.24	4.54	0.22	0.075
P5	0.54	4.84	0.21	0.071

near-optimal case (DC = 0.09 and $T_p = 1.16$). We also note that for pulsed cases with very small duty cycle (DC < 0.05), the film cooling coverage is severely affected by the overwhelming amount of the crossflow compared to the coolant. Also for lower pulsation periods than $T_p = 1.16$ the overall film cooling effectiveness slightly decreases, but the physical mechanisms in the flow remain similar to the first case. Thus clearly, optimal conditions exists for the pulsation parameters, and the mechanisms controlling this are related to the dynamics near the jet-hole exit.

4.3 Film Cooling Response Surface. In Fig. 14, the contour lines of the space- and time-averaged film cooling effectiveness versus DC and T_p are shown. The global optimum is shown by point P1 and its design parameters are at DC = 0.14 and $T_p = 1.16$, which are close to those of the first case discussed in the previous section including the mechanisms responsible for such a behavior. Local optimums are denoted by points P2 to P5. The coordinate of points P1–P5 are their respective values of averaged film cooling effectiveness are given in Table 2.

From the computational point of view an important observation is the presence of local optimums. This nonconvex behavior of the objective function versus the design variables renders the gradient-based optimization strategies inappropriate for this problem, since the gradient-based algorithms will converge to a local optimum depending on the initial guess. This can be partially remedied by using different initial guesses. However, for the current problem each initial guess leads to several expensive DNS simulations. Nevertheless, certainty in obtaining the global optimum cannot be guaranteed in such approaches. Moreover the direct numerical simulations required in gradient-based approaches, have to be carried out in sequence due to the inherent dependence of the updated guess to previous iterations. In contrast, in the current approach all sample points are independent of each other and all simulations can be carried out concurrently, resulting in a significant scale up in the total computation performance.

Another advantage of the current approach, although not exploited in the this study, lies in the fact that the obtained response surface can play the role of a *surrogate model* and can be utilized in different design scenarios, such as optimization cases where the objective function is the film cooling effectiveness with the amount of the coolant penalized with different factors, or the amount of ingestion penalized and so on. Note that once the response surface is obtained, investigating different optimization problems can be carried out very quickly without incurring the computational cost of the DNS.

5 Conclusions

In this work, we investigated the influence of duty cycle and pulsation frequency on film cooling effectiveness for a 35-deg inclined jet in crossflow with a plenum attached to the delivery pipe. We have presented an efficient computational strategy that combines high-fidelity simulations and construction of a response surface in the design space to find the optimal forcing parameters that maximizes the film cooling effectiveness. We carried out 73 direct numerical simulations and obtained the response surface of the averaged film cooling effectiveness as a function of the two design variables of duty cycle and pulsation period for a wide range of DC $\in [0.05, 1]$ and $T_p \in [0.5, 5]$. In summary the findings of this study are:

(1) The optimal film cooling effectiveness occurs in the lower-left quadrant of the DC $- T_p$ design space, and at lower duty cycles (DC = 0.14) and higher frequencies ($St \sim 1$). During the off-period of coolant injection, flow adjustments near the delivery tube include ingestion of the mainstream flow into the tube and the propagation of this ingested front that pushes the coolant in the delivery tube to be squeezed out from the downstream edge of the hole. Thus coolant continues to spill out during the off-period, stays close to the surface, and provides improved coverage. For these cases a double-deck vortical structures were detected, with a hairpin vortex in the upper deck riding on top of a counter rotating vortex pair in the lower deck. The vertical velocity induced by each pair of vortices is small, leading to an attached coolant to the surface.
(2) High duty cycles result in forming distinct vortex rings that are detached from the surface and lead to increased entrainment of the crossflow and thus, poor coverage.
(3) High pulsation periods causes the penetration of the crossflow to the delivery-tube trailing surface and causes a significant temperature rise in the delivery tube and an unfavorable effect on the film cooling effectiveness.
(4) At lower pulsation periods, the ingested gas does not penetrate all the way to the trailing surface of the delivery tube, and does not cause an increase in the trailing wall temperature inside the tube.
(5) Several local optimums were found, rendering the gradient-based optimization strategies inadequate for the current problem.

Acknowledgment

This work was supported by a grant from AFOSR and a grant from the DEPSCoR-AFOSR programs. This support is gratefully acknowledged. S.A. also appreciates the support from the

National Science Foundation (NSF) in the preparation of this manuscript. The computations were performed on Louisiana Optical Network Initiative (LONI) systems at Louisiana State University.

Nomenclature

BR = blowing ratio
D = jet diameter
DC = duty cycle
p = pressure
P_i = polynomial order of the expansion in ξ_i direction
Pr = Prandtl number
Q = number of quadrature points
Re = Reynolds number
St = nondimensional pulsation frequency
T_c = coolant temperature
T_h = hot gas temperature
T_p = pulsation period
$\mathbf{u}$ = velocity vector
U_∞ = crossflow velocity
w = width of the blade
$w^{(i)}$ = i^{th} quadrature weight
$\mathbf{x}$ = Cartesian coordinate
γ_j = L^2-norm of Legendre polynomial
Δt_{off} = time portion of the cycle that the jet in off
Δt_{on} = time portion of the cycle that the jet in on
η = spanwise- and time-averaged film cooling effectiveness
$\tilde{\eta}$ = overall film cooling effectiveness
θ = normalized temperature
Θ^P = one dimensional Clenshaw–Curtis grid with $P+1$ nodes
$\Theta^{(P_1,P_2)}$ = two dimensional Clenshaw–Curtis grid with P_1+1 nodes in ξ_1-direction and P_2+1 nodes in ξ_2-direction
$\boldsymbol{\xi}$ = design parameter
$\boldsymbol{\xi}^{(i)}$ = i^{th} quadrature point
τ = time percentage during a cycle
$\phi_i(\xi)$ = univariate Legendre polynomial of degree i
$\boldsymbol{\phi}_r(\boldsymbol{\xi})$ = multidimensional Legendre polynomial of degree r
$(,)$ = inner product
$\underline{(.)}$ = Fourier coefficient in polynomial expansion
$\overline{(.)}$ = time-averaged
$(.)_N$ = projected to a space of polynomial of degree N
$\|(.)\|$ = norm induced by inner product
$\gamma_j\ L^2 -$ norm of Legendre polynomial

References

[1] Bogard, D. G., and Thole, K. A., 2006, "Gas Turbine Film Cooling," J. Propul. Power, **22**(2), pp. 249–270.

[2] Bunker, R. S., 2005, "A Review of Shaped Hole Turbine Film-Cooling Technology," ASME J. Heat Transfer, **127**, pp. 441–453.

[3] Lutum, E., and Johnson, B. V., 1999, "Influence of the Hole Length-to-Diameter Ratio on Film Cooling With Cylindrical Holes," ASME J. Turbomach., **121**(2), pp. 209–216.

[4] Acharya, S., Tyagi, M., and Hoda, A., 2006, "Flow and Heat Transfer Predictions for Film Cooling," Ann. N.Y. Acad. Sci., **934**(1), pp. 110–125.

[5] Acharya, S., and Tyagi, M., 2003, "Large Eddy Simulation of Film Cooling Flow From an Inclined Cylindrical Jet," ASME Paper No. GT2003-38633.

[6] Iourokina, I., and Lele, S., 2005, "Towards Large Eddy Simulation of Film-Cooling Flows on a Model Turbine Blade With Free-Stream Turbulence," AIAA Paper No. 2005-670.

[7] Peet, Y., and Lele, S. K., 2008, "Near Field of Film Cooling Jet Issued Into a Flat Plate Boundary Layer: LES Study," ASME Paper No. GT2008-50420.

[8] Guo, X., Schroder, W., and Meinke, M., 2006, "Large-Eddy Simulations of Film Cooling Flows," Comput. Fluids, **35**(6), pp. 587–606.

[9] Renze, P., Schroder, W., and Meinke, M., 2008, "Large-Eddy Simulation of Film Cooling Flows at Density Gradients," Int. J. Heat Fluid Flow, **29**(1), pp. 18–34.

[10] Coulthard, S. M., Volino, R. J., and Flack, K. A., 2007, "Effect of Jet Pulsing on Film Cooling—Part I: Effectiveness and Flow-Field Temperature Results," ASME J. Turbomach., **129**(2), pp. 232–246.

[11] Ekkad, S. V., Ou, S., and Rivir, R. B., 2006, "Effect of Jet Pulsation and Duty Cycle on Film Cooling From a Single Jet on a Leading Edge Model," ASME J. Turbomach., **128**(3), pp. 564–571.

[12] El-Gabry, L. A., and Rivir, R. B., 2012, "Effect of Pulsed Film Cooling on Leading Edge Film Effectiveness," ASME J. Turbomach., **134**(4), p. 041005.

[13] Muldoon, F., and Acharya, S., 2009, "DNS Study of Pulsed Film Cooling for Enhanced Cooling Effectiveness," Int. J. Heat Mass Transfer, **52**(13–14), pp. 3118–3127.

[14] Bidan, G., Vezier, C., and Nikitopoulos, D. E., 2013, "Study of Unforced and Modulated Film-Cooling Jets Using Proper Orthogonal Decomposition—Part II: Forced Jets," ASME J. Turbomach., **135**(2), p. 021038.

[15] Warburton, T., 1999, "Spectral/hp Methods on Polymorphic Multi-Domains: Algorithms and Applications," Ph.D. thesis, Brown, Providence, RI.

[16] Karniadakis, G. E., Israeli, M., and Orszag, S. A., 1991, "High-Order Splitting Methods for the Incompressible Navier–Stokes Equations," J. Comput. Phys., **97**(2), pp. 414–443.

[17] Karniadakis, G. E., and Sherwin, S. J., 2005, *Spectral/hp Element Methods for Computational Fluid Dynamics*, Oxford University Press, New York.

[18] Xiu, D., 2007, "Efficient Collocational Approach for Parametric Uncertainty Analysis," Comm. Comp. Phys., **2**(2), pp. 293–309.

[19] Clenshaw, C. W., and Curtis, A. R., 1960, "A Method for Numerical Integration on an Automatic Computer" Numerische Mathematik, **2**(1), pp. 197–205.

[20] Battles, Z., and Trefethen, L., 2004, "An Extension of Matlab to Continuous Functions and Operators," SIAM J. Comput., **25**(5), pp. 1743–1770.

[21] Bidan, G., Vezier, C., and Nikitopoulos, D. E., 2013, "Study of Unforced and Modulated Film-Cooling Jets Using Proper Orthogonal Decomposition—Part I: Unforced Jets," ASME J. Turbomach., **135**(2), p. 021037.

[22] Smirnov, A., Shi, S., and Celik, I., 2001, "Random Flow Generation Technique for Large Eddy Simulations and Particle-Dynamics Modeling," ASME J. Fluids Eng., **123**(2), pp. 359–371.

[23] Sau, R., and Mahesh, K., 2008, "Dynamics and Mixing of Vortex Rings in Crossflow," J. Fluid Mech., **604**, pp. 389–409.

[24] Haven, B. A., and Kurosaka, M., 1997, "Kidney and Anti-Kidney Vortices in Crossflow Jets," J. Fluid Mech., **352**(1997), pp. 27–64.